**Atmospheric
Measurement
Techniques
Discussions**

Volcanic SO$_2$ and SiF$_4$ visualization and their ratio monitored using 2-D thermal emission spectroscopy

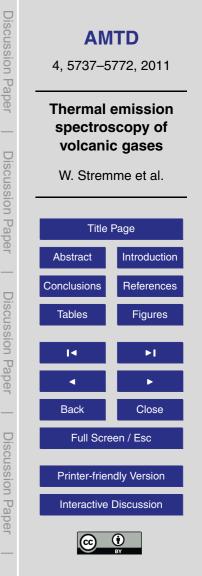**W. Stremme[1], A. Krueger[1,2], R. Harig[2], and M. Grutter[1]**

[1]Centro de Ciencias de la Atmósfera, Universidad Nacional Autónoma de México, Mexico City, Mexico
[2]Technische Universität Hamburg-Harburg, Hamburg, Germany

Correspondence to: M. Grutter (grutter@unam.mx)

Discussion Paper | Discussion Paper | Discussion Paper | Discussion Paper

Title Page

Abstract | Introduction

Conclusions | References

Tables | Figures

|◄ | ►|

◄ | ►

Back | Close

Full Screen / Esc

Printer-friendly Version

Interactive Discussion

Abstract

The composition and emission rates of volcanic gas plumes provide insight of the geo-logic internal activity, atmospheric chemistry, aerosol formation and radiative processes around it. Observations are necessary for 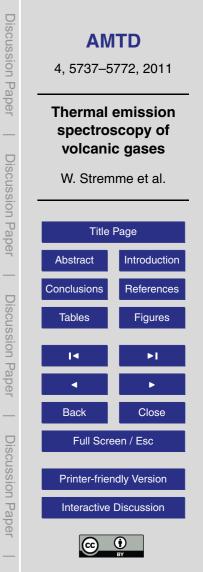public security and the aviation industry. Ground-based thermal emission infrared spectroscopy, which uses the radiation of the volcanic gas itself, allows for continuously monitoring during day and night from a save distance. We present measurements on Popocatépetl volcano based on thermal emis-sion spectroscopy during different campaigns between 2006–2009 using a Scanning Infrared Gas Imaging System (SIGIS). The experimental set-up, measurement geome-tries and analytical algorithms are described. The equipment was operated from a safe distance of 12 km from the volcano at two different spectral resolutions: 0.5 and 4 cm^{-1}. The 2-dimensional scanning capability of the instrument allows for an on-line visualization of the volcanic SO_2 plume, animation and determination of its propaga-tion speed. SiF_4 was also identified in the infrared spectra recorded at both resolutions. The SiF_4/SO_2 molecular ratio can be calculated from each image and used as a highly useful parameter to follow changes in volcanic activity. A small Vulcanian eruption was monitored during the night of 16 to 17 November 2008 which was confirmed from the strong ash emission registered around 01:00 a.m. LST (Local Standard Time) and a pronounced SO_2 cloud was registered. Enhanced SiF_4/SO_2 ratios were observed before and after the eruption. A validation of the results from thermal emission mea-surements with those from absorption spectra of the moon taken at the same time, as well as an error analysis, are presented. The inferred propagation speed from se-quential imagees is used to calculate the emission rates at different distances from the crater.
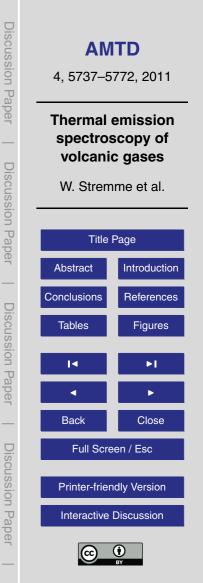
1 Introduction

Volcanoes are known to emit large amounts of gases into the atmosphere and contribute with 10–15 % of the global anthropogenic sulfur emissions (Halmer, 2002). The gas composition of these volcanic plumes are not well understood and differ for each volcano (Aiuppa, 2009). SO_2 from volcanoes has been detected by remote sensing methods both from the ground and from space. Its strong absorptions in the UV have been widely used by COSPEC and now more frequently by DOAS instruments to monitor its fluxes. Satellite-based instruments such as the SCHIAMACHY and OMI, have also been successful in detecting volcanic plumes from space. In the infrared, global monitoring by thermal emission measurements is now possible by sounders with enough spectral resolution such as the TES and IASI instruments (Clarisse et al., 2008). From the ground, infrared studies of the volcanic plume composition have mostly used the solar absorption technique but also open-path and passive FTIR spectroscopy.

Fourier Transform Infrared (FTIR) spectroscopy from the ground has been applied in vulcanology for the last two decades (Notsu et al., 1993; Mori et al., 1993; Francis et al., 1996, 1998; Love et al., 1998; Burton et al., 2001; Goff et al., 2001; Duffell et al., 2001) and many more as for example the recent measurements on Popocatépetl by Grutter et al. (2008) and Stremme et al. (2011). Passive spectroscopy works without controlling the radiation source and can be further distinguished in (A) absorption spectroscopy, which uses the sun, moon or hot rocks as light source and (B) thermal emission spectroscopy, using the radiation emitted by the target gas itself, which acts therefore as the light source. These geometries are depicted in the sketch provided in Fig. 1. While absorption spectroscopy needs for the special condition that source, plume and sensor are in one line, thermal emission spectroscopy only requires for a free sight of the plume. However, for a quantitative analysis of the gases, an accurate radiometric calibration is needed and the temperature (T-profile) along the line-of sight of the background, plume and foreground need to be known or well estimated. A

measurement along the direction C shown in Fig. 1, which is at the same elevation but barely missing the plume up-wind, as will be shown in this work, can aid in the analysis significantly.

According to our knowledge thermal emission spectroscopy to characterize volcanic emissions was applied for the first time in 1996 by Love et al. (1998, 2000) and Goff et al. (2001). From thermal emission spectroscopy, SO_2, SiF_4, H_2O, CO_2 (Goff et al., 2001) and even HCl (Love et al., 2000) have been determined in volcanic gas plumes. However, good H_2O and CO_2 results have proven to be difficult to obtain because of their high atmospheric background. SiF_4 in volcanic gas was first detected by Francis et al. (1996) at the Italian volcano Vulcano and the largest relative SiF_4 content was found at Satsuma-Iwojima volcano, Japan (Mori et al., 2002). Love et al. (1998) suggested that the increasing SiF_4 content measured in Popocatépetl might be related with the Vulcanian-type eruptions measured then and the SiF_4/SO_2 ratio is thought to be an indicator of explosive activity since (McGonigle, 2005). In a recent work, solar absorption measurements of Popocatépetl during an explosion and quiescent degassing showed a systematic difference in the HCl/SO_2, HF/SO_2 and SiF_4/HF molecular ratios (Stremme et al., 2011). It was suggested that SO_2/HF ratios change and increase in explosions due to presence of gas with origin from fresh magma from the depth, while SiF_4/HF ratios can increase due to a cooling of the stored gas near the surface.

In this work we present measurements of the thermal volcanic-plume radiation with a fully automated Scanning Infrared Gas Imaging System (Harig et al., 2005) and new retrieval strategies which allow for simultaneous monitoring of SO_2 and SiF_4. As the determined slant columns are captured in two dimensional images, each scan or plume snapshot produces an average molecular ratio (SiF_4/SO_2) with statistical measure of its significance. This parameter can be used to monitor changes in gas composition day and night, and possibly used as surveillance for future eruptive events. As example the results from an explosive event on the night of 16 to 17 November 2009 are presented. Also the propagation velocity is calculated from the images and the emission rates of these gases can be determined (Supplement S.3).
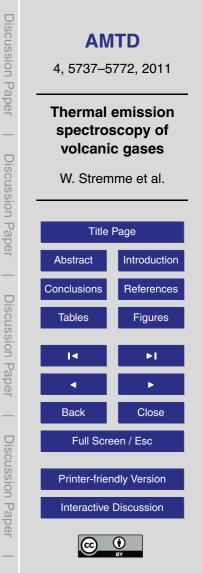
2 Instrumentation

The Scanning Infrared Gas Imaging System (SIGIS) used is comprised of an interferometer (OPAG 22, Bruker Daltonics, Leipzig, Germany), an azimuth-elevation-scanning mirror actuated by stepper motors, a telescope, a data and video processing and control system with a digital signal processor (DSP), a camera and a personal computer (Fig. 2). For the visualization of gas plumes, the scanning mirror is set sequentially to all positions within the field of regard. The size and direction of the field of regard and the spatial resolution (i.e. the angle between adjacent views) are variable. Each interferogram measured by the instrument is recorded by the DSP system where a Fourier transformation is performed and the spectrum is transferred to the PC. The spectrum is analyzed on-line and the column densities (in ppm m) are visualized as false color images laid over the calibrated video image. For each target compound, an image of the space-resolved coefficient of correlation, the signal-to-noise ratio, the brightness temperature of the background and the difference between the temperature of the ambient air and the brightness temperature of the background are also produced. Simultaneous with the analysis and visualization of one interferogram by the DSP and the PC, the scanning mirror is set to move to the next position where a new interferogram is recorded. After the measurement of the field of regard (all pixels in the observation window) is completed, the column densities of all directions in which a compound has been identified may be calculated and an additional false-color image is displayed (Harig et al., 2005).

For quantitative analyses of slant column densities, a radiometric calibration is necessary. The calibration was realized with spectra recorded at two different temperatures taken from a temperature-controlled blackbody. There is a trade-off when choosing the spectral resolution in order to obtain sufficient information about the target and interference gases with higher resolution and looking to improve the signal-to-noise ratio and speed in the data acquisition gained when using the smaller resolution (Harig, 2004). We present two different data sets using spectral resolutions of 4 and $0.5\,\mathrm{cm}^{-1}$. Fast

measurements with the lower resolution allow for two-dimensional scans (consisting of typically 35 × 20 spectra) to be produced within 2 min and still average 5 interferograms per recorded spectrum (pixel). With the higher spectral resolution, 20 interferograms need to be averaged so that full 2-D-scans would take too long to be completed and would not reflect a snapshot of the volcanic plume. The higher resolution spectra are taken only in the spot-observation mode as described in Sect. 4.

The measurements presented in this work were done from the high-altitude Altzomoni site (19.12, −98.65, 4000 m a.s.l.) at a safe distance of 12 km from the crater.
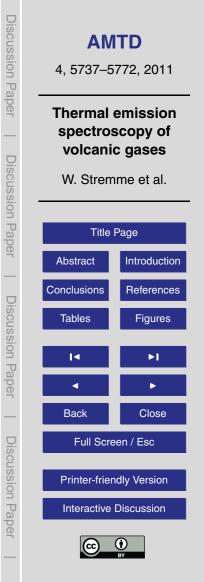
3 Retrieval algorithms

3.1 Algorithm for the 4 cm^{-1} resolution

Passive remote sensing of gas clouds is based on the analysis of infrared radiation absorbed and emitted by the molecules. Figure 1b illustrates the measurement set-up of the method. The radiation measured by the spectrometer contains the spectral signatures of the background of the field of view, the gas cloud, and the atmosphere. The propagation of radiation through the atmosphere is described by the theory of radiative transfer, Eq. (1).

$$L_1 = (1 - \tau_1) B_1 + \tau_1 \left[(1 - \tau_2) B_2 + \tau_2 L_3 \right]. \tag{1}$$

In order to describe the basic characteristics of spectra measured by a passive infrared spectrometer, a simple model with three layers is used (Fig. 1b). Radiation (L_3) from the background (Layer 3), for example the sky (or a surface), propagates through the volcanic plume (Layer 2) and the atmosphere between the plume and the spectrometer (Layer 1). τ_1, τ_2 and B_1, B_2 describe the transmissions and the radiation due to thermal emissions (from Plank's-function) in these layers, respectively. The layers 1 and 2 are assumed homogeneous with regard to all physical and chemical properties within each layer. The radiation containing the signatures of all layers (L_1) is measured
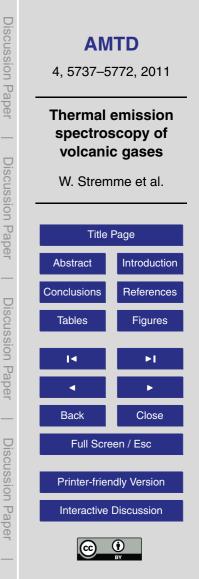
by the spectrometer and the spectra are analyzed by the GeDetekt software developed for the SIGIS (Harig et al., 2009). The reference spectra with different column densities along this path are calculated by the convolution of high resolution transmittance spectra calculated by FASCODE (Smith et al., 1978) using the HITRAN spectral compilation (Rothman et al., 1998) and an instrumental line-shape function. The spectra measured by passive remote sensing spectrometers contain both absorption and emission signatures of the target gas. Baseline shifts in the spectrum that exceed the signal of the target compound due to the radiance of the background and emission inside the spectrometer are also considered. The signatures of atmospheric trace gases, and in particular the signatures of ozone and water vapor, are often greater than the signatures of the target gases. Therefore, the algorithm is optimized to identify and quantify the compounds where the mentioned interference gases and baseline shifts are less sensitive.

The analysis is realized by the approximation of a measured spectrum with a linear combination of reference spectra, which have been converted to brightness-temperature $T_{br}(v)$ (v: frequency in wavenumbers). $T_{br}(v)$ is obtained by the inversion of Planck's function $B(v, T)$ assuming that the thermal radiation is given by the measured intensity of the radiation $L(v)$, Eq. (2).

$$T_{br}(v) = \frac{h\,cv}{k}\left(\ln\left[\frac{2\,h\,c^2\,v^3}{L(v)} + 1\right]\right)^{-1}.\tag{2}$$

For the calculation of the slant-column densities, a plume temperature in the volcanic layer has to be assumed. For the analysis of spectra at $4\,\text{cm}^{-1}$ taken on 16/17 November 2008 the value 275 K was used and for those taken on 28 May 2009 a temperature of 280 K was chosen. Although an exact value of the plume temperature is not known, the visualization and determination of molecular ratios between SiF_4 and SO_2 are quite insensitive to the plume temperature as described by Love et al. (2000) and shown in Sect. 3.2. Possible improvements for the estimation of the plume temperature are discussed in Sect. S.5 (Supplement).

An example of the retrieval results of SO_2 and SiF_4 are shown in Fig. 3. The regions used for the analyses of SO_2 and SiF_4 are 1050–1250 cm^{-1} and 980–1080 cm^{-1}, respectively. The strong SO_2 ν_1-band located around 1150 cm^{-1} can be clearly seen in the spectrum, while that of SiF_4 is weak and slightly larger than the noise in this

5   case. When the fitting parameters from the continuum and other interference gases are removed (blue trace), the SiF_4 signal can more easily be identified.
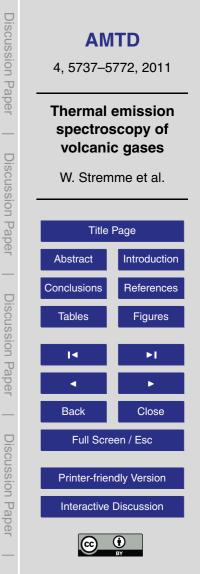
The presence of ash in volcanic plumes can affect the analysis significantly preventing the possibility to quantify the column densities. The emission and absorption of the ash-particles act as a continuum in the spectra similar to that of a solid

10   background like the cone of the volcano. In such cases an analysis using difference spectra (sky-plume) is not possible and a filter is introduced. The integrated intensity between 900 and 1000 cm^{-1} is used to exclude all spectra which are above an empirical intensity-threshold of the received IR-radiation. The scheme works also to exclude the pixels in which the volcano or clouds are in the field-of-view so that more repre-

15   sentative slant columns of the target gases and a corresponding SiF_4/SO_2 ratio can be obtained.

3.2 Algorithm for the 0.5 cm^{-1} resolution

The instrument was designed for thermal emission spectroscopy at different resolutions. For the 0.5 cm^{-1} resolution, the system was set to measure in "spot" mode,

20   which means that it will measure continuously in one direction or it can alternatively switch between two or more directions (pre-defined spots). A new code to retrieve slant columns from individual thermal emission spectra at this resolution was developed. Using a higher resolution has the disadvantage of a lower *S/N* but it helps to separate absorption features of different gases better and might therefore lower sys-

25   tematic errors.

Just as for the lower resolution mode the atmosphere is divided also in 3 layers, each containing a number of relevant gases described by their partial columns and a

mean temperature. The forward model thus is similar as the one described in Sect. 3.1, in Harig et al. (2009) and by Goff et al. (2001). The cross-sections are calculated in a preprocessing step using FASCODE with sufficient high resolution (no apodization) and on a fine grid. Depending on the width of the spectral window, a polynomial of order N is used to simulate the black body radiation from aerosol, ash particles or water drops in the atmosphere and the volcanic plume.

The assumption of the effective temperature in each layer is a critical point. The vertical T-profile from the daily radiosonde launched in Mexico City and the US Standard atmosphere were used for the background layer and we estimated the temperature $T_{\text{bg-layer}}$ with a weighted average using
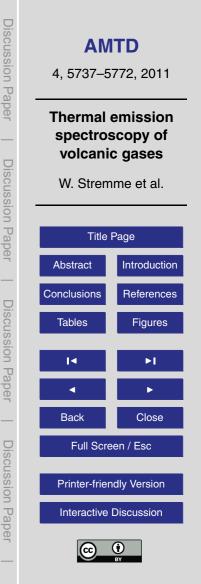
$$
T_{\text{bg-layer}} = \frac{\int T(z)\, \rho_{O_3}(z)\, B(T(z))\, \mathrm{d}z}{\int \rho_{O_3}(z)\, B(T(z))\, \mathrm{d}z}, \tag{3}
$$

where $B(T(z))$ is the black body radiation and $\rho_{O_3}(z)$ the density of the main gas emitting in that region (for example ozone in the SiF_4 retrievals). The foreground temperature is estimated from the instantaneous temperature measured at the observation site. The estimation of the temperature in the volcanic layer is discussed in Supplement part S.4. We assume that the instrumental line-shape can be described by a triangular apodization and the maximal optical path-difference (OPD) was set to 1.8 cm.

The inversion is done using the optimal estimation approach (Rodgers, 1976) and because the forward model is not linear, a Levenberg-Marquard damping mechanism is added. As the number of spectra was small with little computational effort, the retrieval ensures the independence of the results from the starting condition, LM-damping term and convergence criteria through the minimum number of 50 iterations. For each parameter, an a priori value and its co-variance has to be chosen. The choice of the number of parameters, a priori values and constraints is critical. The foreground, volcanic and atmospheric background layers are assumed to be independent and a diagonal a priori covariance matrix was chosen. The $\mathbf{S}_e$-matrix describes the noise in the spectrum but according to the work of von Clarmann et al. (2001), a generalized

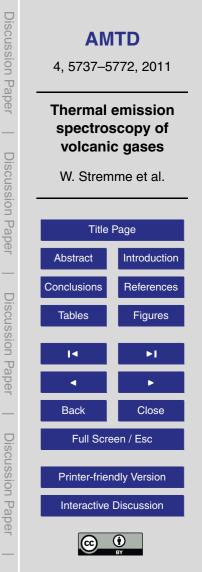S_e-measurement-noise matrix enables the reduction of errors introduced by not fitted of poorly known parameter in the forward model.

The spectral region of 1080–1205 cm^{-1} was used for the SO$_2$ retrieval and the cross-section were calculated using the HITRAN 2004 database. The following temperatures were assumed for the event on 17 November 2008: 300 K (foreground), 280 K (volcanic layer) and 250 K (atmospheric background). A polynomial of order 4 and the gases SO$_2$, O$_3$, CO$_2$, CH$_4$, N$_2$O and H$_2$O are taken into account. SO$_2$ was allowed to adapt freely in the volcanic layer, while CO$_2$, CH$_4$, N$_2$O and H$_2$O are fitted in the foreground layer.

A large source of error in the quantitative determination of the SO$_2$ slant-columns is the interference of water vapor. At 0.5 cm^{-1} the non-Voigt line-shape might be of minor importance, however, the strong variability of its temperature and the presence of water in all three layers makes it difficult to simulate. Even if one could determinate the foreground water-column using the humidity measured in situ, it would be difficult to get rid of spectroscopic problems with the H$_2$O interference, especially with the intense water lines. Therefore, the spectrum was deweighted systematically using the water cross-section as presented in Fig. 4 and which, as mentioned above, is similar like the use of a generalized S_e -matrix (von Clarmann et al., 2001).

The SiF$_4$ cross-sections were calculated from a laboratory spectrum ($T = 300$ K, $P = 1000$ hPa, 55 ppm, 1 m, at 1.0 cm^{-1} resolution) from Hanst et al. (1996) which has also been used by Francis et al. (1996); Love et al. (1998); Mori et al. (2002). The same temperatures as for the SO$_2$-retrieval were assumed for the three layers. In the chosen spectral region, 1020–1040 cm^{-1}, the gases SiF$_4$, O$_3$, CO$_2$, CH$_4$, N$_2$O and H$_2$O were forward simulated, but only SiF$_4$, O$_3$, CO$_2$, H$_2$O and a polynomial of order 2 were fitted. Figure 5 shows the measured and simulated spectra with dominant O$_3$ structures, and a SiF$_4$ signature that is only slightly larger than the residual. As we will see in the results, this signal is sufficiently large to follow the evolution of a SiF$_4$ which is strongly correlated to SO$_2$.

3.3 Algorithm for plume propagation velocity

The combination of the spatial distribution provided by the column density images on one hand, and the information about the temporal change of the slant columns in each pixel obtained by the sequential measurements on the other hand, allows for the calcu-
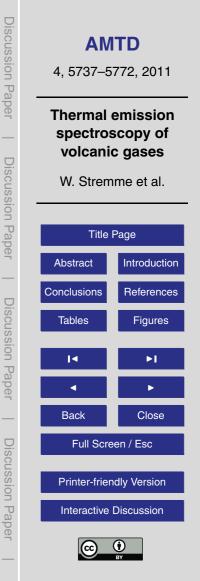5 lation of the velocity and direction of the propagating plume. The approach, described here, reconstructs even a two dimensional (2-D) wind field by solving the continuity equation (Eq. 4) for the column densities.

$$\frac{dcl}{dt} = \nabla(\boldsymbol{v} \cdot cl) + Q. \tag{4}$$

The left term of Eq. (4) represents the time derivation of the SO_2 column density (cl)
10 in each scan-pixel of the false-color image (see Figs. S.6 and S.7 of the Supplement). $\boldsymbol{v}$ is the propagation vector and Q is the source term which describes the gas sources in the image. As the propagation in one time interval might be faster than the pixel size, the images are smoothed before the derivations $\frac{dcl}{dt}$ and ∇cl are calculated. Therefore, not just the information of the neighbour pixels are taken into account and the gradi-
15 ents are valid for the whole time interval between two measurements. For a proper wind speed estimation the sample rate of the images must match the Nyquist criteria concerning the structural frequency (observed puff freq.) of the gas plume. This fre- quency can be obtained from the measurements by multiplying the distance between two puffs with the estimated wind speed. It is obvious that only wind speeds can be
20 obtained which are not strong enough for completely refreshing all SO_2 from one frame to the next.

Since the structural frequency of the plume is not constant, the matching of the Nyquist criteria is not guarantied. The following scheme is implemented: First, the time series of the wind-fields are retrieved using a pure smoothing constraint and the
25 spatially averaged wind velocities are calculated. Normaly the direction is very well retrieved, while the absolute wind speed might be off. After the direction is retrieved, the upper boundary is constrained to a wind speed of 2 m/s with this direction and
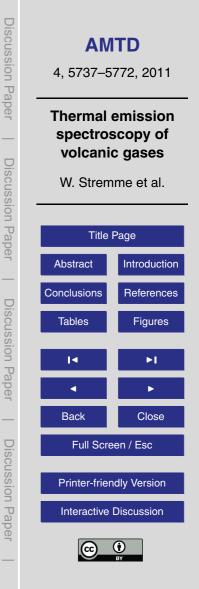
a wind-field is obtained (arrows like in Fig. 12). The SO_2 flux density is calculated by multiplying the wind-field with the column densities. A time series of the fluxes at different distances from the crater results from integrating the flux densities perpendicular to the linear trajectory (near-horizontal line in Fig. 12) separately of both images and multiplying by the wind-field. Two slightly different time series are compared in Fig. 13. One uses the column density from the first frame measured and the second uses the second which is needed for the wind-field calulation. For testing the calulated wind-fields, the time series are cross correlated (Fig. S.3 in the Supplement) and the resulting time shift should match the time difference between the measurements, as is shown in Fig. 13. If this is not the case, a scaling factor for the wind speeds can be calculated and used as a priori information in the final retrieval.

The Eq. (4) describes an ill-posed problem with only $n \times m$ equations, corresponding to the differences in the columns of two sequential frames ($\frac{dcl}{dt}_{11}$, ..., $\frac{dcl}{dt}_{mn}$) and the $>2 \times$ larger solution of the atmospheric state vector $(2 \cdot n \times m) + q$ which is $V = (v^x_{11}, ..., v^x_{mn}, v^y_{11}, ..., v^y_{mn}, Q_1, ..., Q_q)$; the wind components plus the strength of q sources (Fig. S.2 in the Supplement). Therefore, the equation is solved using a Tikhonov smoothing constraint (Tikhonov, 1963) and the following penalty function (Eq. 5) is minimized:

$$P\,F(V) = \left\| \frac{dcl}{dt} - K \cdot V \right\| + \lambda \cdot \left\| (V - V_a) \cdot R \cdot (V - V_a) \right. . \tag{5}$$

V_{ret} is the solution which minimizes the penalty function in the equation above and contains the retrieved wind propagation vectors and the source strength in all pixels. R is the Tikhonov operator (D_1), λ the strength of the constraint and V_a the a priori wind vector. The matrix K contains the gradient introduced in Eq. (4). $R = D^t D$ is constructed from the D_1-operator, applied to the rows and columns of the wind components blockwise (von Clarmann and Grabowski, 2007).
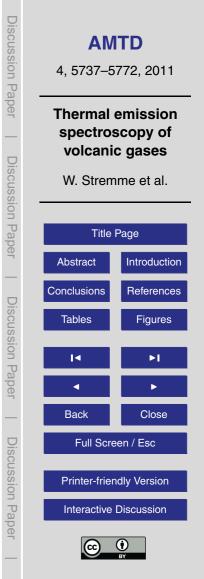
$$D_1 = \begin{pmatrix} 1 & -1 & 0 & \cdots & 0 \\ 0 & 1 & -1 & \ddots & \vdots \\ \vdots & \ddots & \ddots & \ddots & 0 \\ 0 & \cdots & 0 & 1 & -1 \end{pmatrix} \quad (6)$$

R is a smoothing constraint which encourages the neighbored vectors **V** to have similar size and to point in the same direction.

4   Results and discussion

5 Figure 6 shows a typical SO_2 plume from Popocatépetl volcano measured by thermal emission spectroscopy at $4\,cm^{-1}$. The SO_2 was retrieved according to the description made in Sect. 3.1, considering a plume temperature of 265 K. Various puffs are visible in the false-color image and the measured SO_2 slant columns can be integrated over one puff to estimate its SO_2 gas content. The puff in the right hand side of Fig. 6, for
10 example, contains an estimated 4 t of SO_2 when the 2-D area of the puff is integrated, considering a distance of 12 km from the measurement site and a pixel size of 0.028°. The 2-D scans were continuously measured so that the plumes propagation could be animated over several hours (see videos in Supplement S.1 and S.2).

Volcanic SiF_4 slant columns were analyzed from difference spectra at $4\,cm^{-1}$. At
15 favorable conditions like on 28 May 2009, one 2-D scan which lasted around 1.5 min contains enough information to calculate the molecular ratio with a statistical error below 5 % (95 % confidence interval). The results of this scan are presented in Fig. 7. The SiF_4/SO_2 molecular ratio in this particular example is $(1.18 \pm 0.03) \times 10^{-3}$ and the corresponding SO_2 and SiF_4 amounts within the measured window are 12 t and 24 kg,
20 respectively. It is important to note that the near-horizontal viewing arrangement produces a strong interference with ozone and continuum radiation affecting the retrieved slant columns as well as the resulting absolute value of the molecular ratios. The
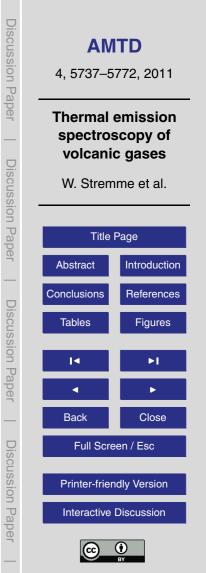
presence of ash and clouds produce additional uncertainties and the reported ratios should therefore be treated carefully. However, it will be shown next that the relative changes in the measured ratios can be important parameters when related to the volcanic activity.

During the night 16/17 November 2008, an explosion occurred around 01:06 a.m. LT (local time) and large amounts of SO_2 and ash were emitted. The SiF_4 retrieval was performed from the difference spectra and still very close to the detection limit (see Sect. 3.1). To improve the signal-to-noise ratio in this event, the retrieved slant column densities of the nearest neighbors were averaged vertically and horizontally by a running average of 4. The results of a sequence are presented in Fig. 8. White areas where the integrated intensity are large (see Sect. 3.1) are filtered out clearly showing the presence of the ash-plume and the contour of the volcano in the third row, a few minutes after the explosion (01:18 LST). The corresponding animation of this sequence is presented as Supplement S.2.

A difference between the spatial distributions of SiF_4 and SO_2 would be interesting to analyze, as recent measurements at Fuego Volcano in Guatemala by Nadeau et al. (2011) with a UV-imaging system found SO_2 emitted through different vents. It is possible that just after the explosion, as seen in the third row of this sequence, the maximum of SiF_4 is propagated earlier towards the right border than SO_2. Although a single snapshot does not provide sufficient arguments for making conclusions, it can be seen from the simultaneous plume animations that this instrument is capable of identifying differences in the spatial distribution of the gases (see S.2 in the Supplement).
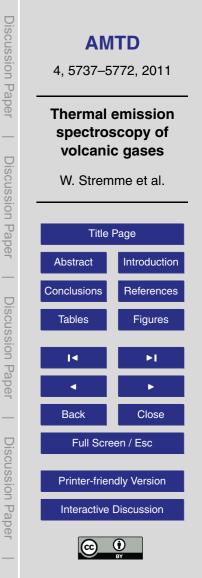
In Fig. 9, the time series of both the integrated IR radiation collected just above the crater and the calculated SiF_4/SO_2 molecular ratios is presented. The time series of the integrated intensity (Fig. 9a) indicates the time and duration of the explosion. Only the values below the threshold, represented by the dashed line, were considered for calculating the gas ratios. One reference spectrum and one radiometric calibration, with a plume temperature assumed at 275 K, were used in the evaluation. These assumptions introduce uncertainties and therefore not the absolute but rather the relative

behavior is interesting to observe. There is a clear increase in the SiF_4/SO_2 ratio not only after the eruption, but also a couple of hours before. The ratio then returns to low values several hours after the explosion.

A general behavior is deduced from the interpretation of Figs. 8 and 9. There is a low emission of gases several hours prior to the explosion. The SiF_4/SO_2 ratio starts to increase 2–3 h before, rises excessively during and just after the event and then drops to low values a few hours later. The emissions of both SO_2 and SiF_4, however, remain strong throughout the next day probably through open-venting.

Slant columns of SO_2 and SiF_4 at $0.5\,cm^{-1}$ were also recorded on 17 November 2008 (spot B in Fig. 1) during almost 1 h and are plotted in Fig. 10. The spectra were recorded ∼16 h after the explosion with optimal conditions for measuring with thermal emission spectroscopy. A large variability observed in the retrieved slant columns is consistent with the puffs observed by Grutter et al. (2008). The SiF_4 and SO_2 columns are, however, changing synchronously. The correlation of both columns including those from the clear sky (spot C in Fig. 1) results in a Pearsons correlation coefficient R^2 of 0.96 and a molecular ratio SiF_4/SO_2 of 0.00140 ± 0.00007 (Fig. 11). Errors are calculated with the 95 % confidence interval, assuming that the ratio is constant and errors in the SiF_4 retrieval are dominant. During the measurement period no significant change in the SiF_4/SO_2 ratio could be observed.

The results from various measurement periods, however, shows a significant variation in the SiF_4/SO_2 molecular ratios during quiescent degassing of Popocatépetl, Table 1. Not all measurements are equally reliable, as the geometry, meteorological conditions and calibration conditions might have differed. Table 1 differentiates between thermal emission measurements made in image mode, as shown in Figs. Figs. 7 and 8, and the spot mode as presented in Figs. 10 and 11. On the morning of 17 November, a few spectra with volcanic gas were recorded near the moon when the measurement site was almost directly below the gas cloud. On 28 May 2009, measurements were recorded before sunrise using the scanning infrared system pointing above the crater while the instrument was located in the hut under more stable conditions.
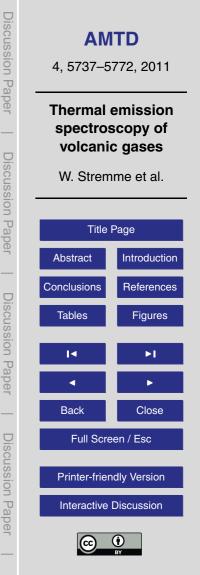
W. Stremme et al.

The comparison of the molecular ratios presented in Table 1 between lunar absorption and thermal emission shows a difference of 0.00078 ± 0.0005. These measurements were taken at the same time and the plume-temperature was adjusted according to the description presneted in Sect. S.4 (Supplement). As the systematic difference is only slightly larger than their uncertainty, the errors are estimated with the 95 % confidence interval, however, the dataset is based on only 6 measurements and in fact one plume measurement and 5 background measurements. As the interference gases and parameters play an important role in the SiF_4 retrievals, a greater set of measured spectra would be helpful. As the slant columns of SO_2 are consistent using the temperature of the environment at 5000 m a.s.l., we assume that there is a small systematic error in the retrieval of SiF_4 (see S.5 in the Supplement). However, not sufficient evidence is available to infer which of both retrievals (thermal emission or absorption) remains slightly biased.

In Fig. 12 we present an example of the plume propagation vectors determined from the equation of continuity described in Sect. 3.3. The arrows in the figure depict both the direction and magnitude of the constrained movement detected by two sequential SO_2 images.

The propagation vectors are useful for quantifying both the direction and velocity of the emitted gases. Fluxes can then be estimated by multiplying the integrated cross-sectional count ($kg\,m^{-1}$) by the velocity ($m\,s^{-1}$). The latter parameter has normally the largest uncertainty, as for example from plume transects performed by DOAS (Grutter et al., 2008). However, this methodology provides a real and on-line determination of both parameters needed for flux calculations. In Fig. 13 we present the result of the emission fluxes calculated at different distances from the crater. It is important to consider that in order to adequately estimate the fluxes, a correction for a projected propagation speed perpendicular to the line-of-sight would be required, which was not performed in this example.
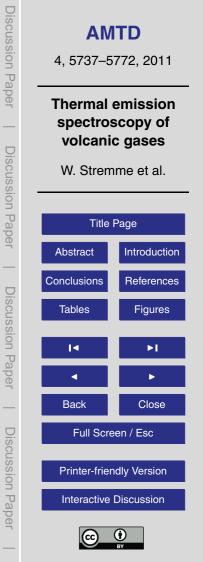
Full Screen / Esc

Printer-friendly Version

Interactive Discussion

5 Conclusions

This work describes how a fully automatized scanning FTIR emission spectrometer can be used for plume visualization of volcanic gases, as well as continuous monitoring of emission ratios at favorable conditions. The instrument operation for thermal emission spectroscopy and the retrieval algorithms are described. The instrument can also be deployed to monitor other atmospheric relevant sources and in the case of continuous operation for volcanic surveillance, its automatized capability presents many benefits and opportunities allowing for:

- the detection of large column densities and molecular ratios of specific gases even during the night (with the posibility to warn with an alarm algorithm during an eruptive event),

- a visual representation of the individual volcanic gas plumes (with a large statistical significance from the increased data collection in various atmospheric and volcanic conditions),

- the identification of opportunities for taking solar or lunar absorption spectra of the plume (as when validating results from thermal emission measurements and performing specific studies like in Stremme et al., 2011),

- a detailed reanalysis of special events using individual optimized and adapted retrieval strategies.

The visualization of the SO_2 plume and its animation from longer sequences is presented. The SiF_4 gas relevant for volcanic activity was simultaneously analyzed from the lower resolution spectra and it was possible to visualize its plume for the first time. SiF_4/SO_2 molecular ratios could be determined from the sequential 2-D images at $4\,cm^{-1}$ with detected enhancements before and after an eruptive event. Alternatively, the $0.5\,cm^{-1}$ spectral resolution set in spot-observation mode just above the crater
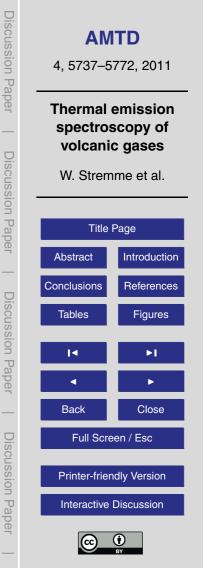
allowed for more information about the individual interferences to be acquired and an error estimation to be performed.

Down-wind plumes can be quatified such as in the false-color images of 28 May 2009 (Fig. 6), where the total SiF_4 and SO_2 contents were found to be 24 kg and 12 t, repec-
tively, the latter being equivalent to the average SO_2 emission of Popocatépetl in 7 min. An algorithm was developed to calculate the wind-fields from the column density results in sequential images. From that it was possible to estimate a wind propagation velocity perpendicular to the field-of-view and the resulting gas fluxes.

On 17 November 2008, there was an opportunity to measure the volcanic plume both
by thermal emission and lunar absorption at the same time. The plume temperature for the thermal emission retrieval was fitted in order to match the slant columns of the lunar absorption result and the temperature came out to be that of the environment at that particular altitude. This result is somewhat expected and supports for future assumptions to be made when no coincident absorption measurements are possible.

The large distance of 12 km to the crater and the near-horizontal field-of-view used in this study has some advantages, as the plume moved relatively slow and there was a possibility to monitor plumes in different altitudes and directions with almost the same elevation angle. However, that the atmospheric interference gases have large slant columns is a disadvantage. Therefore, the spectral signature of gases with
smaller abundances, such as SiF_4, have small *S/N* ratios and can only be analyzed from difference-spectra.

The time series of SiF_4/SO_2 ratios, registered for the night of 16/17 November 2008, revealed a significant increase in SiF_4 before and during a Vulcanian-type eruption. The SiF_4/SO_2 ratio alone, however, might not be a reliable indicator for explosions
and dome cooling, as both the *S/F* atomic ratio and the SiF_4/HF ratio are variable in the volcanic gas. An improvement of the spectrometer using for example a larger telescope together with a broader-range detector (MCT/INSB sandwich detector with a bandpass-filters) would allow to simultaneously measure HCl at 2800 cm^{-1} (Love et al., 2000; Gross et al., 2010). Multi-element detectors in the near future could also

improve the aquisition speed and avoid the need of a scanning mirror. Also, as has been mentioned, the possibility of long-term monitoring with this technique would allow for gaining better emission statistics, which together with other parameters, wind conditions and seismic data, could provide new insights in the behavior of volcanic emission and activity.

Supplementary material related to this article is available online at:
http://www.atmos-meas-tech-discuss.net/4/5737/2011/amtd-4-5737-2011-supplement.zip.

References

Aiuppa, A.: Degassing of halogens from basaltic volcanism: Insights from volcanic gas observations, Chem. Geol., 263, 99–109, doi:10.1016/j.chemgeo.2008.08.022, 2009. 5739

Burton, M. R., Oppenheimer, C., Horrocks, L. A., and Francis, P. W.: Diurnal changes in volcanic plume chemistry observed by lunar and solar occultation spectroscopy, Geophys. Res. Lett., 28, 843–846, doi:10.1029/2000GL008499, 2001. 5739

Clarisse, L., Coheur, P. F., Prata, A. J., Hurtmans, D., Razavi, A., Phulpin, T., Hadji-Lazaro, J., and Clerbaux, C.: Tracking and quantifying volcanic SO_2 with IASI, the September 2007 eruption at Jebel at Tair, Atmos. Chem. Phys., 8, 7723–7734, doi:10.5194/acp-8-7723-2008, 2008. 5739

Duffell, H., Oppenheimer, C., and Burton, M.: Volcanic gas emission rates measured by solar occultation spectroscopy, Geophys. Res. Lett., 28, 3131–3134, doi:10.1029/2000GL012425, 2001. 5739

Thermal emission spectroscopy of volcanic gases

W. Stremme et al.

Title Page

Abstract	Introduction
Conclusions	References
Tables	Figures

|◄ | ►|

◄ | ►

Back | Close

Full Screen / Esc

Printer-friendly Version

Interactive Discussion

Francis, P., Chaffin, C., Maciejewski, A., and Oppenheimer, C.: Remote determination of SiF_4 in volcanic plumes: A new tool for volcano monitoring, Geophys. Res. Lett., 23, 249–252, doi:10.1029/96GL00022, 1996. 5739, 5740, 5746

Francis, P., Burton, M. R., and Oppenheimer, C.: Remote measurements of volcanic gas compositions by solar occultation spectroscopy, Nature, 396, 567–570, doi:10.1038/25115, 1998. 5739

Goff, F., Love, S. P., Warren, R. G., Counce, D., Obenholzner, J., Siebe, C., and Schmidt, S. C.: Passive infrared remote sensing evidence for large, intermittent CO_2 emissions at Popocatépetl volcano, Mexico, Chem. Geol., 177, 133–156, doi:10.1016/S0009-2541(00)00387-9, 2001. 5739, 5740, 5745

Gross, K. C., Bradley, K. C., and Perram, G. P.: Remote Identification and Quantification of Industrial Smokestack Effluents via Imaging Fourier-Transform Spectroscopy, Environ. Sci. Technol., 44, 9390–9397, doi:10.1021/es101823z, 2010. 5754

Grutter, M., Basaldud, R., Rivera, C., Harig, R., Junkerman, W., Caetano, E., and Delgado-Granados, H.: SO_2 emissions from Popocatépetl volcano: emission rates and plume imaging using optical remote sensing techniques, Atmos. Chem. Phys., 8, 6655–6663, doi:10.5194/acp-8-6655-2008, 2008. 5739, 5751, 5752

Halmer, M.: The annual volcanic gas input into the atmosphere, in particular into the stratosphere: a global data set for the past 100 years, J. Volcanol. Geoth. Res., 115, 511–528, doi:10.1016/S0377-0273(01)00318-3, 2002. 5739
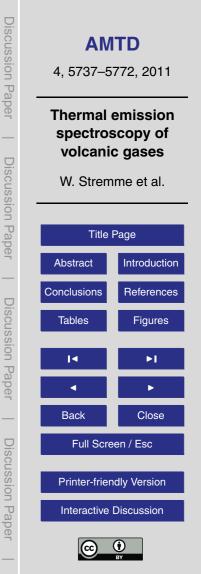
Hanst, P., Hanst, S., and Williams, G.: Infrared Spectra for Quantitative Analysis of Gases, QASoftDatabase, Infrared Analysis, Inc., Anaheim, CA, 1996. 5746

Harig, R.: Passive Remote Sensing of Pollutant Clouds by Fourier-Transform Infrared Spectrometry: Signal-to-Noise Ratio as a Function of Spectral Resolution, Appl. Optics, 43, 4603–4610, doi:10.1364/AO.43.004603, 2004. 5741

Harig, R., Rusch, P., Dyer, C., Jones, A., Moseley, R., and Truscott, B.: Remote measurement of highly toxic vapors by scanning imaging Fourier-transform spectrometry, in: Society of Photo-Optical Instrumentation Engineers (SPIE) Conference Series, edited by: Jensen, J. O. and Thériault, J.-M., vol. 5995 of Society of Photo-Optical Instrumentation Engineers (SPIE) Conference Series, 316–327, doi:10.1117/12.631730, 2005. 5740, 5741

Harig, R., Rusch, P., Peters, H., Gerhard, J., Braun, R., Sabbah, S., and Beecken, J.: Field-portable imaging remote sensing system for automatic identification and imaging of hazardous gases, in: Society of Photo-Optical Instrumentation Engineers (SPIE) Conference
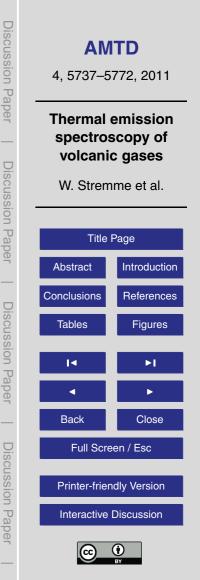
Thermal emission spectroscopy of volcanic gases

W. Stremme et al.

Title Page

Abstract | Introduction

Conclusions | References

Tables | Figures

|◀ | ▶|

◀ | ▶

Back | Close

Full Screen / Esc

Printer-friendly Version

Interactive Discussion

Series, vol. 7475 of Society of Photo-Optical Instrumentation Engineers (SPIE) Conference Series, doi:10.1117/12.830627, 2009. 5743, 5745

Love, S. P., Goff, F., Counce, D., Siebe, C., and Delgado, H.: Passive infrared spectroscopy of the eruption plume at Popocatépetl volcano, Mexico, Nature, 396, 563–567, doi:10.1038/25109, 1998. 5739, 5740, 5746

Love, S. P., Goff, F., Schmidt, S. C., Counce, D., Pettit, D., Christensen, B., and Siebe, C.: Passive infrared spectroscopic remote sensing of volcanic gases: ground-based studies at White Island and Ruapehu, New Zealand, and Popocatépetl, Mexico, vol. 116 of Geophys. Monogr., Am. Geophys. Union, 117–138, 2000. 5740, 5743, 5754

McGonigle, A. J. S.: Volcano remote sensing with ground-based spectroscopy, Philos T. Roy. Soc. Lond. A, 363, 2915–2929, doi:10.1098/rsta.2005.1668, 2005. 5740

Mori, T., Notsu, K., Tohjima, Y., and Wakita, H.: Remote detection of HCl and SO_2 in volcanic gas from Unzen volcano, Japan, Geophys. Res. Lett., 20, 1355–1358, doi:10.1029/93GL01065, 1993. 5739

Mori, T., Sato, M., Shimoike, Y., and Notsu, K.: High SiF_4/HF ratio detected in Satsuma-Iwojima volcano's plume by remote FT-IR observation, Earth Planets Space, 54, 249–256, 2002. 5740, 5746

Nadeau, P. A., Palma, J. L., and Waite, G. P.: Linking volcanic tremor, degassing, and eruption dynamics via SO_2 imaging, Geophys. Res. Lett., 38, 1304–1308, doi:10.1029/2010GL045820, 2011. 5750

Notsu, K., Mori, T. G. G. I., Tohjima, Y., and Wakita, H.: Infrared spectral radiometer: a new tool for remote measurement of SO_2 of volcanic gas, Geochem. J., 27, 361–366, 1993. 5739

Rodgers, C. D.: Retrieval of Atmospheric Temperature and Composition From Remote Measurements of Thermal Radiation, Rev. Geophys. Space Ge., 14, 609–624, 1976. 5745

Rothman, L. S., Rinsland, C. P., Goldman, A., Massie, S. T., Edwards, D. P., Flaud, J., Perrin, A., Camy-Peyret, C., Dana, V., Mandin, J., Schroeder, J., McCann, A., Gamache, R. R., Wattson, R. B., Yoshino, K., Chance, K., Jucks, K., Brown, L. R., Nemtchinov, V., and Varanasi, P.: The HITRAN Molecular Spectroscopic Database and HAWKS (HITRAN Atmospheric Workstation): 1996 Edition, J. Quantit. Spectrosc. Ra., 60, 665–710, doi:10.1016/S0022-4073(98)00078-8, 1998. 5743

Smith, H. J. P., Dube, D. J., Gardner, M. E., Clough, S. A., and Kneizys, F. X.: FASCODE: Fast Atmospheric Signature CODE (spectral transmittance and radiance), 1978. 5743

Thermal emission spectroscopy of volcanic gases

W. Stremme et al.

Title Page

Abstract | Introduction

Conclusions | References

Tables | Figures

|◀ | ▶|

◀ | ▶

Back | Close

Full Screen / Esc

Printer-friendly Version

Interactive Discussion

Stremme, W., Ortega, I., Siebe, C., and Grutter, M.: Gas composition of Popocatépetl Volcano between 2007 and 2008: FTIR spectroscopic measurements of an explosive event and during quiescent degassing, Earth Planet. Sc. Lett., 301, 502–510, doi:10.1016/j.epsl.2010.11.032, 2011. 5739, 5740, 5753

Tikhonov, V. I.: Reviews of Topical Problems: Peaks of Random Processes, Soviet Physics Uspekhi, 5, 594–611, doi:10.1070/PU1963v005n04ABEH003439, 1963. 5748

von Clarmann, T. and Grabowski, U.: Elimination of hidden a priori information from remotely sensed profile data, Atmos. Chem. Phys., 7, 397–408, doi:10.5194/acp-7-397-2007, 2007. 5748

von Clarmann, T., Grabowski, U., and Kiefer, M.: On the role of non-random errors in inverse problems in radiative transfer and other applications, J. Quant. Spectrosc. Ra., 71, 39–46, 2001. 5745, 5746

Title Page

Abstract | Introduction

Conclusions | References

Tables | Figures

|◄ | ►|

◄ | ►

Back | Close

Full Screen / Esc

Printer-friendly Version

Interactive Discussion

Table 1. Results of the SiF_4/SO_2 ratios obtained from different measurement strategies.

Event	Mode	Resol. (cm^{-1})	$SiF_4/SO_2 \times 10^{-3}$	R^2	N
11/17/08 early morning	thermal emission image	4	0.39 ± 0.02	–	1 frame
11/17/08 early morning	lunar absorption	0.5	1.68 ± 0.02	0.67	57
11/17/08 early morning	thermal emission spot	0.5	0.90 ± 0.45	0.66	6
11/17/08 morning	solar absorption $v_1 + v_3$	0.5	2.56 ± 0.30	0.65	213
11/17/08 morning	solar absorption v_1	0.5	2.54 ± 0.26	0.66	156
11/17/08 afternoon	thermal emission spot	0.5	1.40 ± 0.07	0.96	114
05/28/09 early morning	thermal emission image	4	1.18 ± 0.03	0.80	828
05/28/09 early morning	thermal emission spot	0.5	1.50 ± 0.18	0.69	110

Fig. 1. (a) Different measurement geometries in the infrared using (A) solar/lunar absorption spectroscopy, (B, C) thermal emission spectroscopy at and beside the plume, respectively. SO_2 from Popocatépetl can readily be detected from thermal IR spectra and imaged by performing 2-D scans around the crater. A plume-sky difference (C–B) was used to analyze the weak SiF_4 signal and cope with the strong interferences. **(b)** Sketch of the three layers (background, plume and foreground) used in the forward model to simulate the spectra.

Fig. 2. (a) Schematics of the SIGIS construction with corresponding components and **(b)** illustration of the instrument scanning a 2-D image represented by the field of regard (red grid).
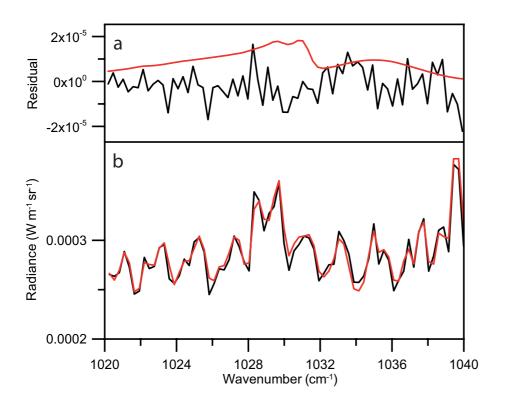
Fig. 3. Spectral regions where SO$_2$ **(a)** and SiF$_4$ **(b)** are retrieved at 4 cm^{-1} resolution. Lower plots: The difference of a plume spectrum and a reference-sky spectrum are shown in black and the corresponding fits in green. The same is plotted above for the spectra (blue) and fits (red) when all other fit parameters (continuum radiation and interference gases) are removed. Above: the residuals of the fits for each retrieval window.
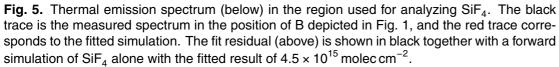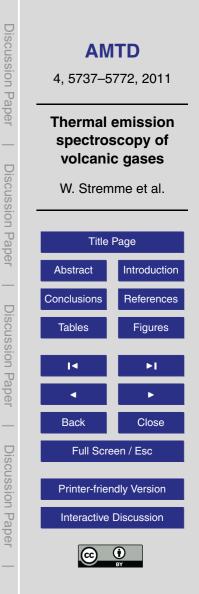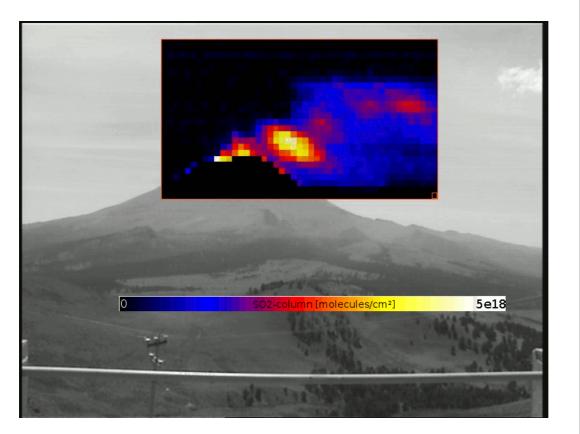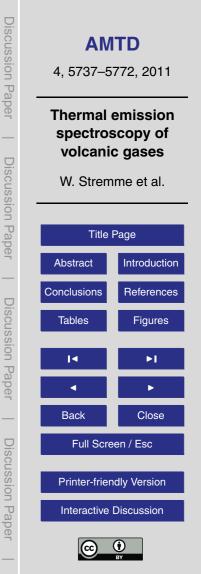
Fig. 4. Thermal emission spectrum (below) around the SO$_2$ ν_1-band on 17 November 2008 at 17:45 LT. The black trace is the measured spectrum in the direction of (B) depicted in Fig. 1, and the red trace corresponds to the fitted simulation. The H$_2$O cross-section (above) is used for systematically deweighting the water lines in the analysis.

Fig. 5. Thermal emission spectrum (below) in the region used for analyzing SiF$_4$. The black trace is the measured spectrum in the position of B depicted in Fig. 1, and the red trace corresponds to the fitted simulation. The fit residual (above) is shown in black together with a forward simulation of SiF$_4$ alone with the fitted result of 4.5×10^{15} molec cm^{-2}.

Fig. 6. A typical SO$_2$ plume from Popocatépetl volcano measured from the Altzomoni site on 17 March 2006. The slant column densities can be obtained with the on-line evaluation software after proper radiometric calibration and plume temperature estimation.

Fig. 7. Left panel: on-line analysis of the SO_2 and SiF_4 plumes displaying the retrieved slant columns in false-colored images. Difference spectra were calculated using the outermost left pixel as background and a temperature of 280 K was assumed for the evaluation. The sum of the slant columns within this window corresponds to 12 t of SO_2 and 24 kg of SiF_4. Right panel: correlation between the column-densities of both gases in the scanned window resulting in a SiF_4/SO_2 ratio of $(1.80 \pm 0.034) \times 10^{-3}$.
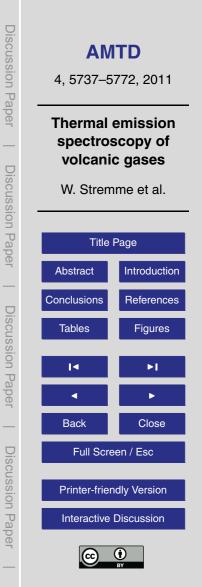
Fig. 8. Visualization of the **(a)** SO_2 and **(b)** SiF_4 slat columns retrieved at different times during the night of 16 to 17 November 2008. The integrated intensity around 900–1000 cm^{-1} is shown in **(c)**. The correlations from plots in d) are calculated only from pixels with lower intensities – those with color in **(c)**. A wind direction change is evident from the last row and one reference spectrum as clear sky was used for all the analysis (see video S.2 in the Supplement).

Title Page

Abstract | Introduction

Conclusions | References

Tables | Figures

|◀ | ▶|

◀ | ▶

Back | Close

Full Screen / Esc

Printer-friendly Version
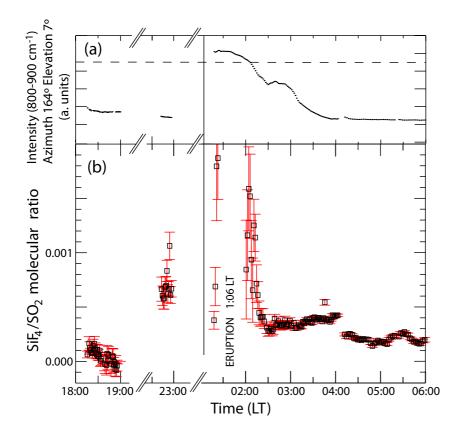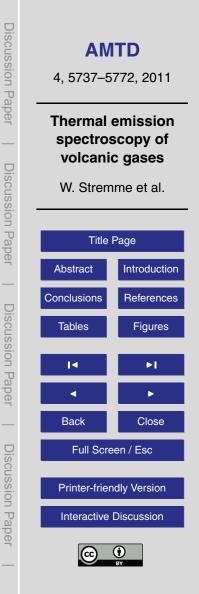
Interactive Discussion

Fig. 9. Time-series of **(a)** the integrated radiation collected from above the crater and **(b)** the SiF_4/SO_2 molecular ratio (squares) before and after the eruptive event that took place between 01:06 and 01:45 LT of 17 November 2008. The dashed line indicates the threshold chosen to filter-out data for calculating molecular ratios.
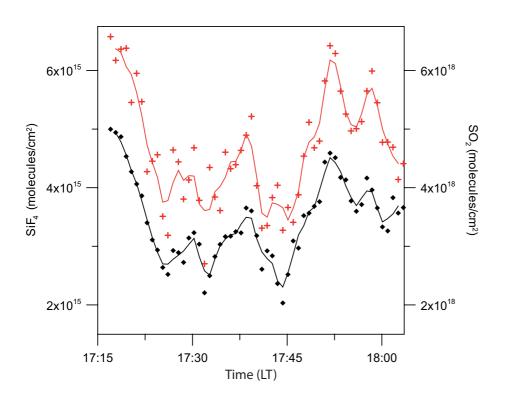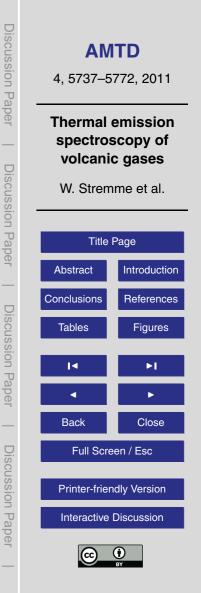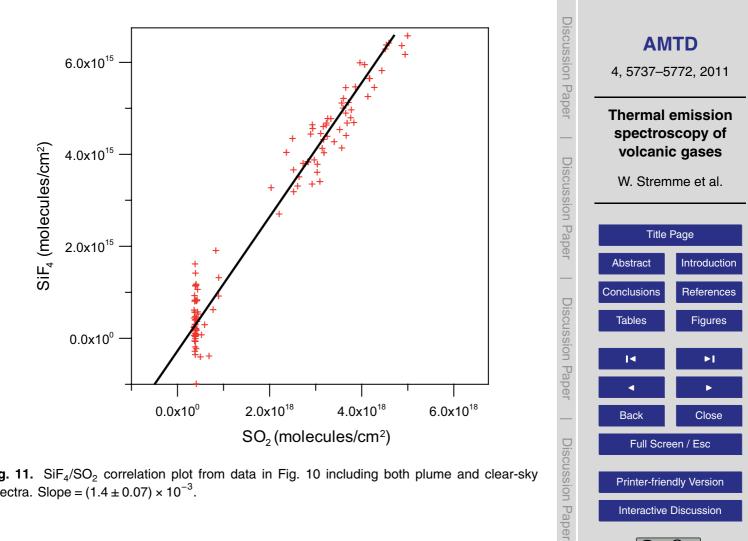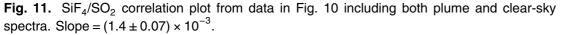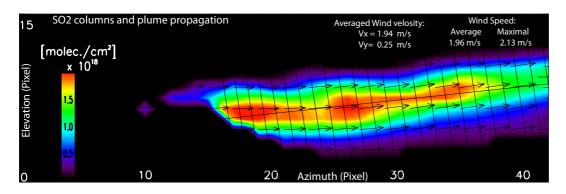
Full Screen / Esc

Printer-friendly Version

Interactive Discussion

Fig. 10. Time series of the SO_2 (black diamonds) and SiF_4 (red crosses) slant columns obtained from thermal emission spectra recorded at $0.5\,cm^{-1}$ resolution on 17 November 2008.
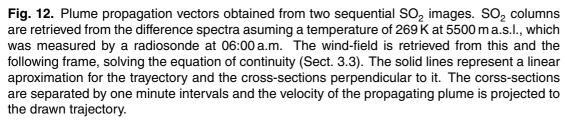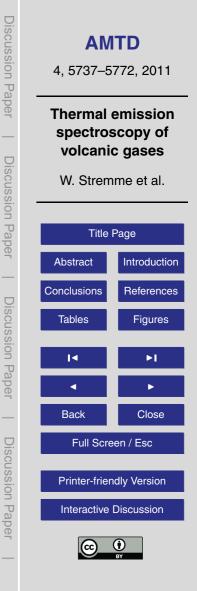
Fig. 11. SiF_4/SO_2 correlation plot from data in Fig. 10 including both plume and clear-sky spectra. Slope $= (1.4 \pm 0.07) \times 10^{-3}$.

Fig. 12. Plume propagation vectors obtained from two sequential SO$_2$ images. SO$_2$ columns are retrieved from the difference spectra asuming a temperature of 269 K at 5500 m a.s.l., which was measured by a radiosonde at 06:00 a.m. The wind-field is retrieved from this and the following frame, solving the equation of continuity (Sect. 3.3). The solid lines represent a linear aproximation for the trayectory and the cross-sections perpendicular to it. The corss-sections are separated by one minute intervals and the velocity of the propagating plume is projected to the drawn trajectory.
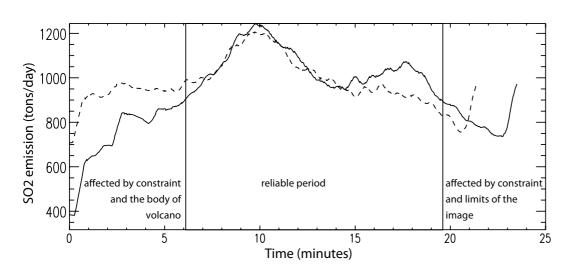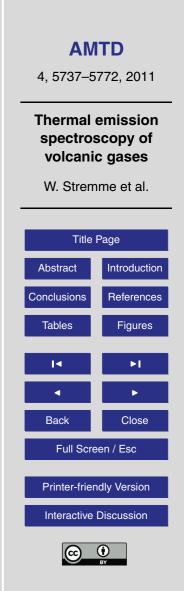
Fig. 13. Calculated SO$_2$ emission (tons/day) at different distances from the crater represented by the cross-sections drawn in Fig. 12 and using the reconstructed wind-field. The distance is shown as the time of its propagation after the starting point of the linear trajectory (Fig. 12). The solid line shows the flux calulated using the first image of SO$_2$-columns and the dashed line shows the flux at the same time, but based on the next SO$_2$-image. The reconstruction of the wind-field is done using a constraint which limites its spatial resolution. Especially near the crater, the dispersion of the SO$_2$ plume is not very well represented by the retrieved wind-field and the SO$_2$ emission/flux is underestimated (more or less below 5 min). A similar effect occours at the other end of the image. In the center of the plume, where the linear trajectory is well represented, both SO$_2$-flux estimations are consistent.